NANO EXPRESS   **Open Access**

Rational Design of Ni(OH)$_2$ Hollow Porous Architecture for High-Sensitivity Enzyme-Free Glucose Sensor

Liangliang Tian[1], Gege He[1,2], Meijing Chen[1*], Jinbiao Wang[1*] , Yucen Yao[1] and Xue Bai[1]

Abstract

Ni(OH)$_2$ electrocatalysts have acquired lots of research attentions as ideal substitutes for noble metals. However, their electrocatalytic performance still cannot meet the demands for applications due to the difficulties in electron transfer and mass transport. According to kinetics principle, the construction of hollow structure is regarded as an effective method to achieve outstanding electrocatalytic performance. In this work, Ni(OH)$_2$ hollow porous architecture (Ni(OH)$_2$ HPA) was simply synthesized through a coordinating etching and precipitating (CEP) method for the building of enzymatic-free glucose sensors. Ni(OH)$_2$ HPA presents large specific surface area (SSA), ordered diffusion channels, and structure stability. As a detection electrode for glucose, Ni(OH)$_2$ HPA exhibits eminent electroactivity in terms of high sensitivity (1843 μA mM^{-1} cm^{-2}), lower detection limit (0.23 μM), and short response time (1.4 s). The results demonstrate that Ni(OH)$_2$ HPA has practical applications for construction of enzymatic-free electrochemical sensors. The design of hollow structure also provides an effective engineering method for high-performance sensors.

Keywords: Ni(OH)$_2$, Hollow structure, Coordinating etching and precipitating, Glucose detection, Electrochemical sensor

Background

Glucose detection is very important in clinical biochemistry, food processing, and environmental monitoring. Developing a fast and reliable sensing method for glucose is an urgent demand for these applications [1–3]. Many techniques have been developed for this purpose, such as surface plasmon resonance [4], Fehling reagent method [5], optical rotation method [6], fluorescence [7], and electrochemistry [8]. Among these techniques, electrochemical methods have attracted more attentions owing to its high sensitivity, simplicity, low cost, and extraordinary low detection limit [9].

It is well known that the electrocatalytic activity of the working electrode determines the performance of the electrochemical sensors. Therefore, the design of electrode materials is vital for electrochemical sensors. Recently, transition metal hydroxides have been widely researched in this field due to the advantages of large reserves, low cost, and high activity derived from the

redox of metal composition [10]. Typically, Ni(OH)$_2$ was recognized as an ideal catalyst for glucose due to the redox couple (Ni^{3+}/Ni^{2+}) in alkaline medium. Although the metal components of Ni(OH)$_2$ can be used to restore the highly active electrons provided by the redox, their catalytic activity is still not high enough to meet the large-scale industrial production and people's living needs because of the difficulties in electron transfer and mass transport.

Inspired by the intimate connection between kinetics and microstructures (shape, size, component), scientists have already built different structured nanomaterials that are good for electrocatalytic dynamics, since the properties of the nanomaterials are usually structure-dependent [11]. Hollow porous nanostructure, which possesses well-defined interior voids, high specific surface area (SSA), low density, and structure stability, has attracted growing interests in recent years [12]. The available inner cavities effectively prevent active particles from aggregation and accommodate the structural strain accompanied with long-time measurements [13]. Otherwise, the functional shells can offer larger contact area between electrolyte and electrode, provide sufficient active sites, and

* Correspondence: cmjftxlj@163.com; wlsf108@163.com
[1]Research Institute for New Materials Technology, Chongqing University of Arts and Sciences, Chongqing, People's Republic of China
Full list of author information is available at the end of the article

Tian *et al. Nanoscale Research Letters* (2018) 13:342

Page 2 of 9

reduce the length for both mass and electron transport [14]. Furthermore, the porous thin shell also supplies enough diffusion paths for analyte and intermediates, which are good for mass transport process [15]. In conclusion, high-active $Ni(OH)_2$ electrocatalysts can be acquired through the building of hollow porous feature.

Herein, cubic $Ni(OH)_2$ HPA is constructed by a Cu_2O-templated method inspired by the concept of coordinating etching and precipitating (CEP) route [16]. In order to demonstrate the advantages of hollow porous architecture, we comparatively evaluated the electrocatalytic activity of $Ni(OH)_2$ HPA and broken $Ni(OH)_2$ HPA ($Ni(OH)_2$ BHPA) through the detection of glucose. The hollow porous architecture provides larger SSA, more ordered transfer paths, and higher electron transfer efficiency compared to $Ni(OH)_2$ BHPA. Thus, the as-prepared $Ni(OH)_2$ HPA electrode presents higher electrocatalytic activity in terms of higher sensitivity, lower detection limit, and faster response time. The results demonstrate that $Ni(OH)_2$ HPA has potential applications for construction of electrochemical glucose sensors. This facile strategy also provides a valid method in the development of highly efficient nanomaterials for electrochemical sensors.

Methods/Experimental
Chemicals and Reagents
Copper chloride ($CuCl_2·2H_2O$; ≥ 99.0%), nickel chloride ($NiCl_2·6H_2O$; ≥ 98.0%), sodium thiosulfate ($Na_2S_2O_3·5H_2O$; ≥ 99.0%), polyvinyl pyrrolidone (PVP; $M_w = 40,000$), and sodium hydroxide (NaOH; ≥ 98.0%) were obtained from Chengdu Kelong. Glucose (Glu.; ≥ 99.5%), lactose (Lact.; ≥ 98.0%), sucrose (Sucr.; ≥ 99.5%), fructose (Fruc.; ≥ 99.0%), L-ascorbic acid (AA; ≥ 99.7%), uric acid (UA; ≥ 99.0%), and Nafion solution (5 wt% in mixture of lower aliphatic alcohols and water) were obtained from Sigma-Aldrich.

Synthesis of $Ni(OH)_2$ HPA
Firstly, cubic Cu_2O crystals were prepared following our previous work (Additional file 1: Figure S1) [17]. Then, 10 mg as-prepared cubic Cu_2O crystals and $NiCl_2·6H_2O$ powder (4 mg) were dispersed into a mixed ethanol-water solution (10 mL, volume ratio = 1:1) by ultrasound. Thereafter, 0.33 g PVP powder was added with vigorous stirring for 0.5 h. Then, $Na_2S_2O_3$ (4 mL, 1 M) was added dropwise into the above system. The reaction was proceeded at normal temperature (25 °C) for 3 h. Finally, the products were washed for several times by centrifugation and dried at normal temperature. $Ni(OH)_2$ BHPA was obtained as contrast sample through strong ultrasonic treatment of $Ni(OH)_2$ HPA for 2 h (Additional file 1: Figure S2).

Materials Characterization
The crystal structure and composition of the products were measured by X-ray diffraction (XRD; Rigaku D/Max-2400) and X-ray photoelectron spectrometer (XPS; ESCALAB250Xi). The morphologies of the products were characterized by field emission scanning electron microscope (FESEM; FEI Quanta 250 and Zeiss Gemini 500) and high-resolution transmission electron microscope (HRTEM; FEI F20). The SSA and pore structure were analyzed on Brunauer-Emmett-Teller (BET; Belsort-max).
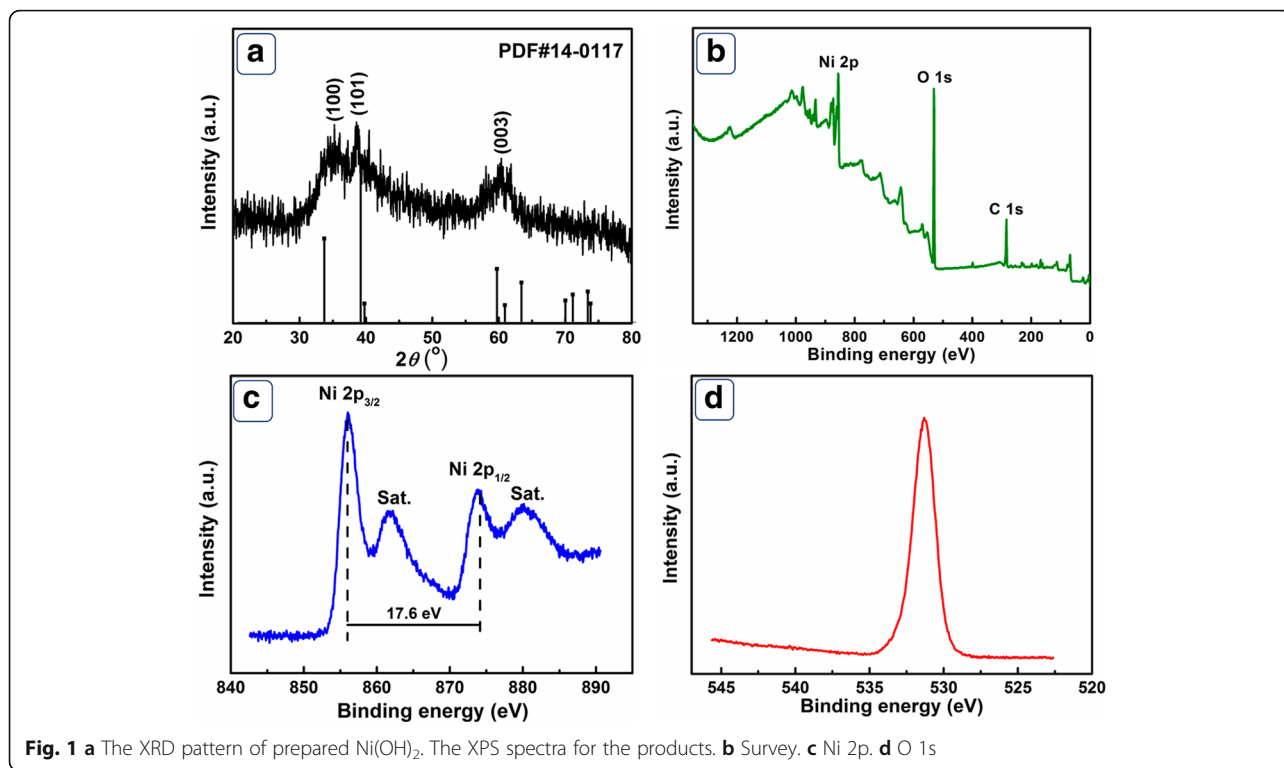
Electrochemical Measurements
All electrochemical measurements were operated on electrochemical workstation (μIII Autolab). The working electrode is prepared by casting Nafion-impregnated $Ni(OH)_2$ HPA (or $Ni(OH)_2$ BHPA) powders onto a glassy carbon electrode (GCE; 3 mm in diameter) at room temperature. Specifically, 5 μL of the suspension (1 mg/ml in 0.05% Nafion solution) is dropped onto the pretreated GCE and dried by flowing N_2. A Pt foil and Ag/AgCl electrode were used as counter electrode and reference electrode, respectively. The electrocatalytic activity of working electrodes was measured by cyclic voltammetry (CV), chronoamperometry (CA), and electrochemical impedance spectroscopy (EIS). EIS data were collected between 0.01 and 100 kHz with a perturbation amplitude of 5 mV.
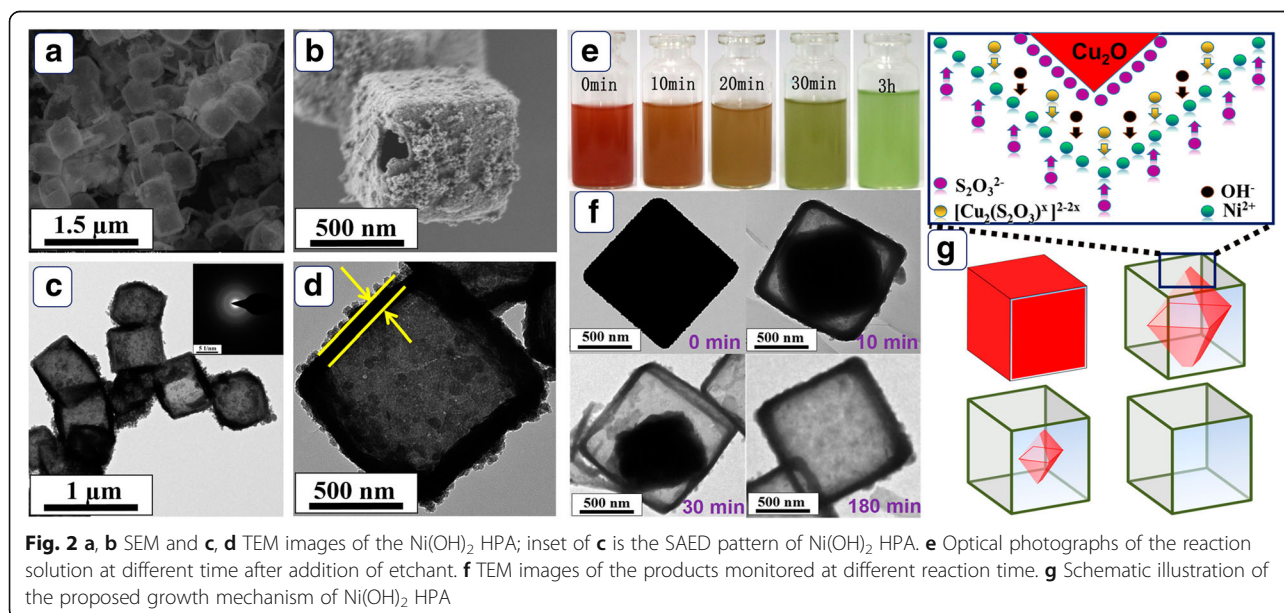
Results and Discussions
Characterizations
The XRD pattern of $Ni(OH)_2$ products was shown in Fig. 1a. The three main diffraction peaks can be assigned to (100), (101), and (003) crystalline planes of hexagonal β-$Ni(OH)_2$ (JCPDS no. 14-0117) [18]. The weak intensity of the diffraction peaks can be attributed to low crystallinity of the products. The purity and composition of the as-prepared $Ni(OH)_2$ were further investigated by XPS. The survey spectrum (Fig. 1b) demonstrates O 1s and Ni 2p peaks, revealing the main composition of the products. As displayed in Fig. 1c, the peaks located at 856.1 eV and 873.7 eV can be assigned to Ni $2p_{3/2}$ and Ni $2p_{1/2}$, respectively. A binding energy separation of 17.6 eV is clearly observed, which is the characteristic of β-$Ni(OH)_2$. As displayed in Fig. 1d, the single peak at 531.2 eV corresponds to Ni–O–Ni bond in Ni–OH. By comparing the data with previous XPS studies, the presented Ni and O can be assigned to Ni^{2+} and OH^- in $Ni(OH)_2$, respectively [16]. The analysis of XPS and XRD confirm the successful preparation of $Ni(OH)_2$ phase.

The low-magnification SEM image in Fig. 2a demonstrates a uniform cubic feature of the prepared $Ni(OH)_2$ products. The partly broken cube shown in Fig. 2b confirms the hollow characteristic of $Ni(OH)_2$ HPA.

Tian *et al. Nanoscale Research Letters* (2018) 13:342

Page 3 of 9

Fig. 1 a The XRD pattern of prepared $Ni(OH)_2$. The XPS spectra for the products. **b** Survey. **c** Ni 2p. **d** O 1s
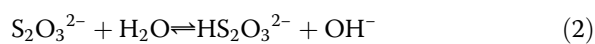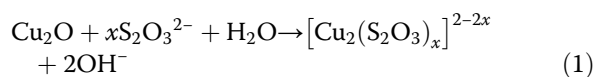
Moreover, the shell of $Ni(OH)_2$ HPA is built through the aggregation of numerous fine nanoparticles, making the shell rough and porous. The TEM images displayed in Fig. 2c further confirms the hollow structure of $Ni(OH)_2$ products. Meanwhile, no significant diffraction ring is observed in selected area electron diffraction (SAED)

pattern, suggesting low crystallinity of $Ni(OH)_2$ HPA. This result agrees well with the observation of XRD. Clearly investigated in Fig. 2d, the $Ni(OH)_2$ hollow cube has an edge length of ~ 600 nm and a shell thickness of ~ 50 nm. The hollow porous structure provides large SSA and amounts of diffusion channels, which may

Fig. 2 a, **b** SEM and **c**, **d** TEM images of the $Ni(OH)_2$ HPA; inset of **c** is the SAED pattern of $Ni(OH)_2$ HPA. **e** Optical photographs of the reaction solution at different time after addition of etchant. **f** TEM images of the products monitored at different reaction time. **g** Schematic illustration of the proposed growth mechanism of $Ni(OH)_2$ HPA

benefit the mass diffusion process, resulting in satisfactory electrocatalytic activity.

The products prepared at different reaction stages were centrifuged and observed to realize the relevant formation principle. As observed in Fig. 2e, the color of the reaction system gradually turns light green and precipitates generate at the same time. As shown in Fig. 2f, the interior Cu_2O cores are gradually etched to octahedron after the addition of $S_2O_3^{2-}$ ions. The Cu_2O octahedrons finally disappear with the increase of reaction time. Combined with TEM images, the formation principle is illustrated in Fig. 2g. Apparently, $S_2O_3^{2-}$ ions adsorbed around Cu_2O cubes play versatile roles during the formation process of $Ni(OH)_2$ HPA: (i) soluble $[Cu_2(S_2O_3^{2-})_x]^{2-2x}$ complex is formed through the combination of Cu^+ ions and $S_2O_3^{2-}$ (reaction (1)) and simultaneously OH^- ions are released. (ii) The hydrolysis of $S_2O_3^{2-}$ also releases OH^- ions (reaction (2)). (iii) Reactions (1) and (2) facilitate the formation of $Ni(OH)_2$ (reaction (3)) [19]. Regarding the kinetics factors, the diffused OH^- ions from the interior determine the formation of $Ni(OH)_2$ shell. Furthermore, the etching of Cu_2O is correlated to the transport of $S_2O_3^{2-}$ from exterior into internal space [20]. Synchronously controlling of OH^- and $S_2O_3^{2-}$ transport leads to the formation of well-defined $Ni(OH)_2$ HPA.

$$Cu_2O + xS_2O_3^{2-} + H_2O \rightarrow [Cu_2(S_2O_3)_x]^{2-2x} + 2OH^- \tag{1}$$

$$S_2O_3^{2-} + H_2O \rightleftharpoons HS_2O_3^{2-} + OH^- \tag{2}$$

$$Ni^{2+} + 2OH^- \rightarrow Ni(OH)_2 \tag{3}$$

The adsorption-desorption isotherm curve and the pore size distribution of $Ni(OH)_2$ HPA and $Ni(OH)_2$ BHPA are shown in Fig. 3. The SSA of $Ni(OH)_2$ HPA is calculated to be 54.72 m^2 g^{-1} based on the desorption curve, which is much larger than that of $Ni(OH)_2$ BHPA (10.34 m^2/g). The decrease of SSA can be attributed to the destruction of

hollow structure and aggregation of the destroyed particles after ultrasonic treatment. The pore size distribution of $Ni(OH)_2$ HPA and $Ni(OH)_2$ BHPA both show regions below 10 nm, revealing the presence of nanopores between $Ni(OH)_2$ nanoparticles. The pore size distribution of $Ni(OH)_2$ HPA (inset of Fig. 3a) displays two concentrated regions of 20–40 nm and 60–85 nm, demonstrating the presence of micropores and mesopores. The micropores and mesopores might make the ion diffusion to active sites easier [21]. In the case of $Ni(OH)_2$ BHPA (inset of Fig. 3b), a weak concentrated distribution is only investigated between 20 and 40 nm, indicating that the pore distribution of $Ni(OH)_2$ BHPA is partly disordered. The decrease of SSA and destruction of ordered pore size may lead to difficulties in kinetics, resulting in poor electrocatalytic activity.

Electrochemical Measurements

The electrocatalytic activity of $Ni(OH)_2$ HPA and $Ni(OH)_2$ BHPA was studied through the detection of glucose in 0.1 M NaOH. Figure 4a shows the CVs of $Ni(OH)_2$ HPA and $Ni(OH)_2$ BHPA electrodes with and without 0.5 mM glucose. Obviously, the redox peak current of $Ni(OH)_2$ HPA (curve I) is higher than $Ni(OH)_2$ BHPA (curve III) due to larger SSA. Upon addition of 0.5 mM glucose, the current responses of $Ni(OH)_2$ HPA electrode (curve II) are higher than $Ni(OH)_2$ BHPA electrode (curve IV). Otherwise, $Ni(OH)_2$ HPA electrode shows lower onset potential (0.41 V) than that of $Ni(OH)_2$ BHPA electrode (0.44 V). The higher electrocatalytic activity of $Ni(OH)_2$ HPA can be attributed to high electron transfer rate, large SSA, and ordered pore structure provided by the hollow porous architecture. The electrocatalysis of glucose on $Ni(OH)_2$ HPA electrode is driven by $Ni(OH)_2$/NiOOH redox couple in alkaline medium on the basis of following reactions [22], and the corresponding schematic diagram is illustrated in Scheme 1.
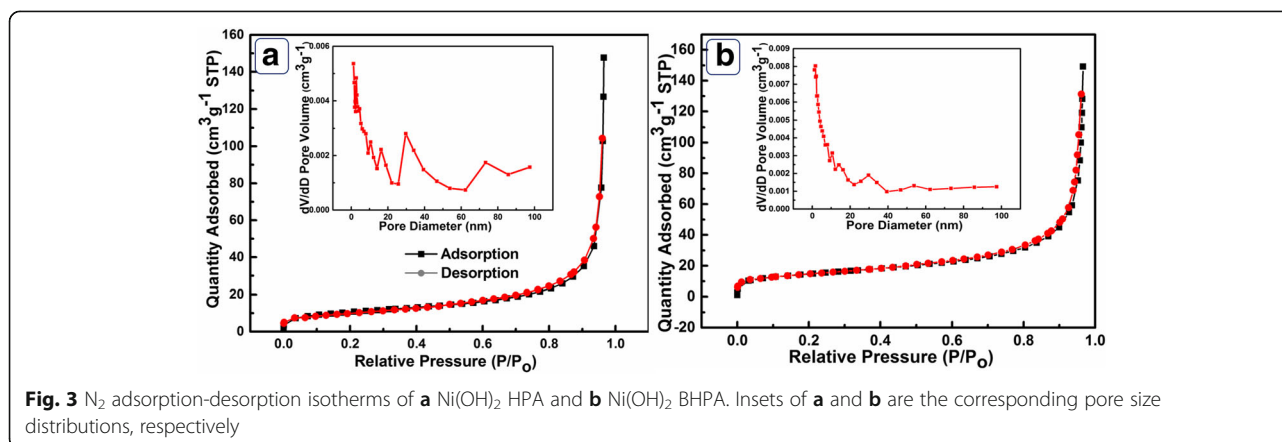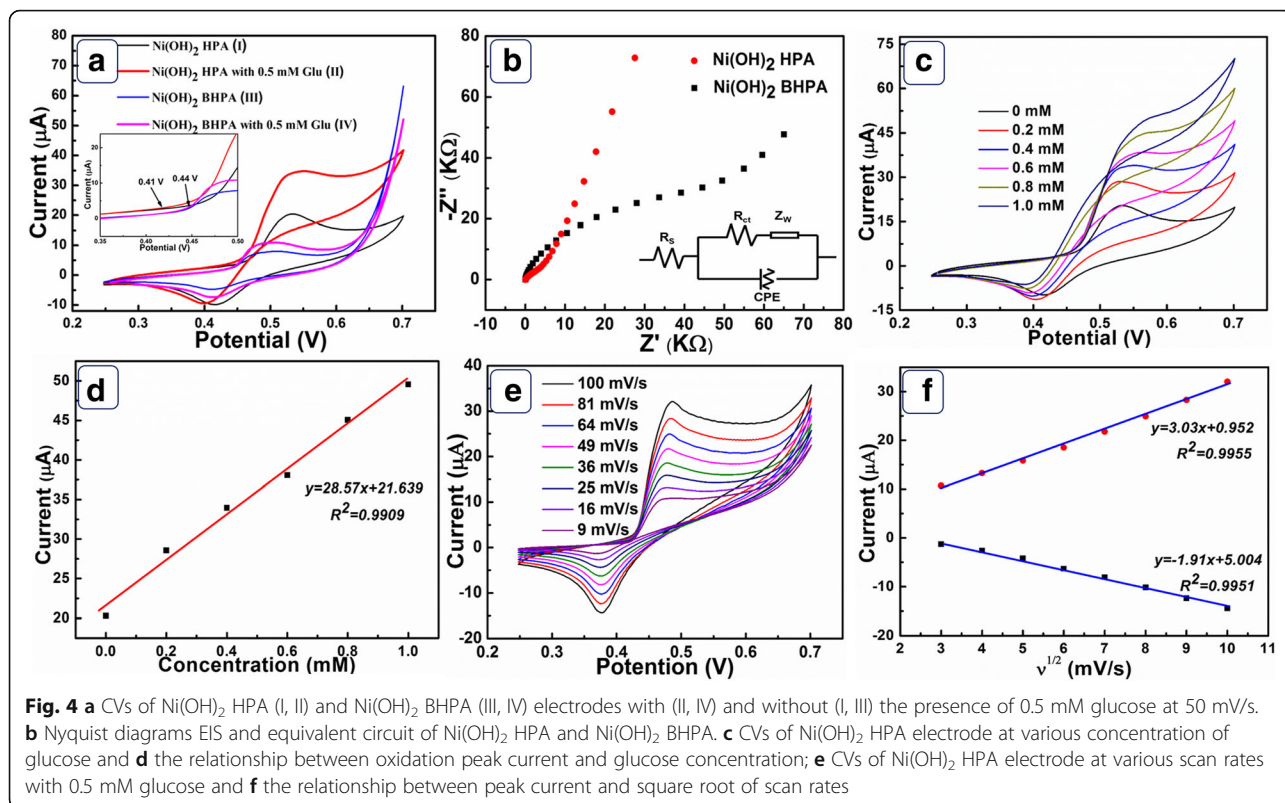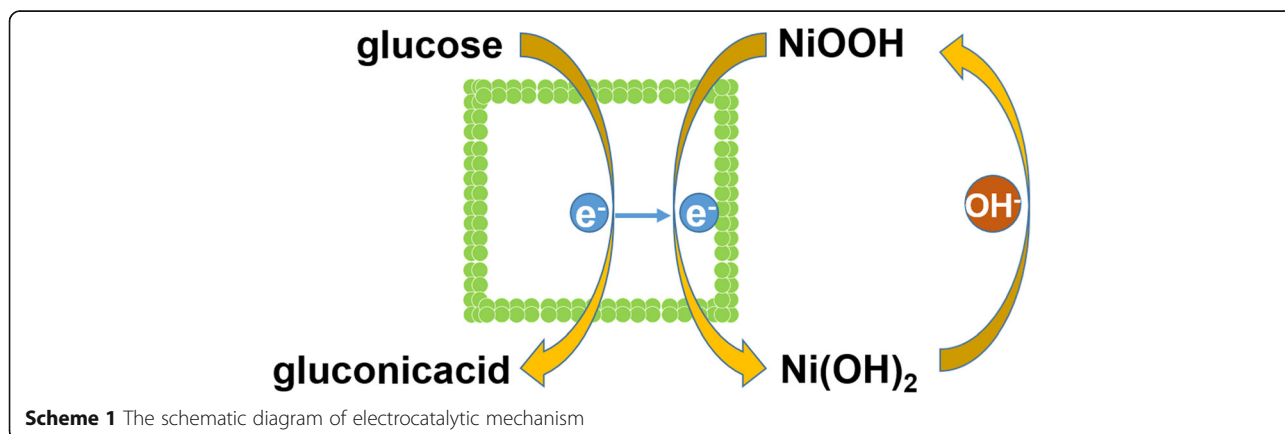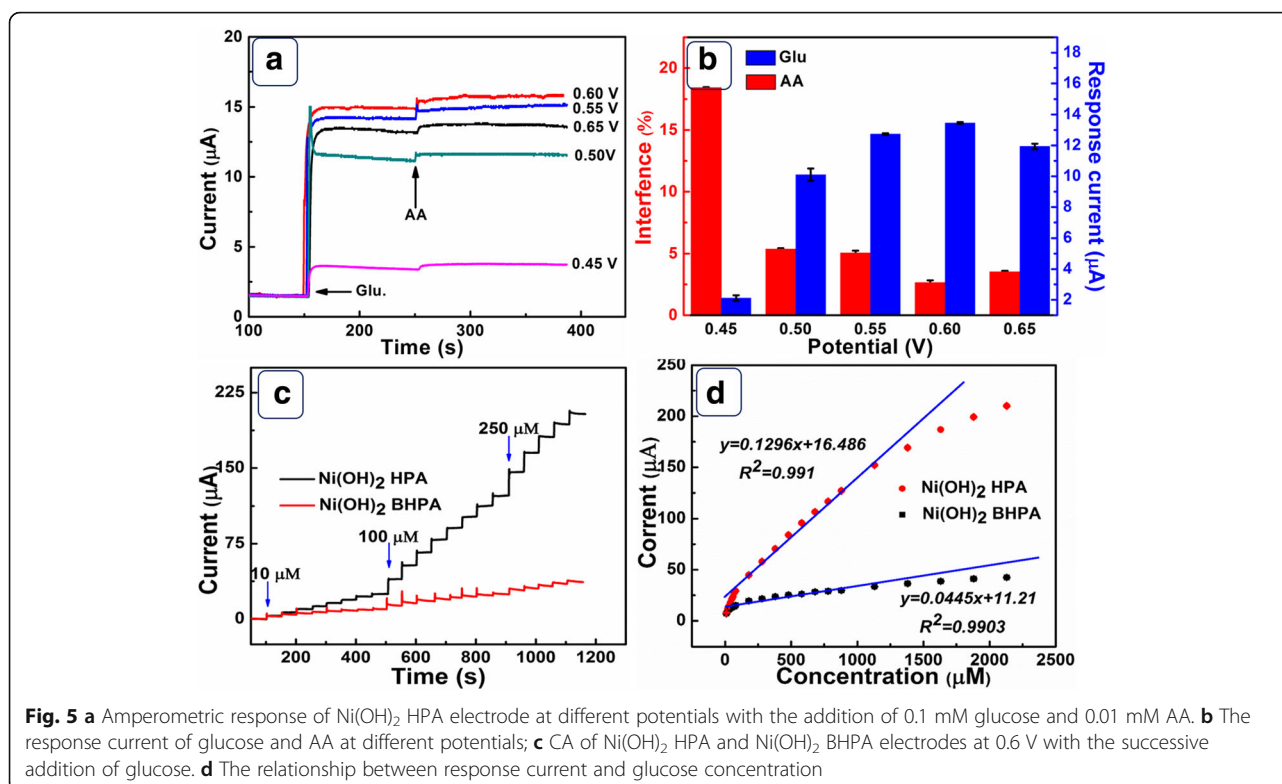

Fig. 3 N_2 adsorption-desorption isotherms of **a** $Ni(OH)_2$ HPA and **b** $Ni(OH)_2$ BHPA. Insets of **a** and **b** are the corresponding pore size distributions, respectively

Fig. 4 a CVs of Ni(OH)$_2$ HPA (I, II) and Ni(OH)$_2$ BHPA (III, IV) electrodes with (II, IV) and without (I, III) the presence of 0.5 mM glucose at 50 mV/s. **b** Nyquist diagrams EIS and equivalent circuit of Ni(OH)$_2$ HPA and Ni(OH)$_2$ BHPA. **c** CVs of Ni(OH)$_2$ HPA electrode at various concentration of glucose and **d** the relationship between oxidation peak current and glucose concentration; **e** CVs of Ni(OH)$_2$ HPA electrode at various scan rates with 0.5 mM glucose and **f** the relationship between peak current and square root of scan rates

$$Ni(OH)_2 + OH^- \rightarrow NiOOH + H_2O + e^- \quad (4)$$

$$NiOOH + glucose \rightarrow Ni(OH)_2 + gluconic\,acid \quad (5)$$

In order to confirm the kinetic advantages of hollow porous feature, EIS spectra of Ni(OH)$_2$ HPA and Ni(OH)$_2$ BHPA were measured (Fig. 4b). The EIS spectrum is characterized by a semicircle in high-frequency and an incline in low-frequency region. As shown in Additional file 1: Table S1, Ni(OH)$_2$ HPA electrode exhibits smaller internal

resistance (Rs) and electron transfer resistance (Rct) than Ni(OH)$_2$ BHPA. Moreover, the Warburg impedance (Zw) of Ni(OH)$_2$ HPA is larger than that of Ni(OH)$_2$ BHPA, indicating more effective mass transfer rate. The difficulties in mass transfer kinetics of Ni(OH)$_2$ BHPA can be ascribed to the destruction of ordered diffusion channels and aggregation of the broken cubes. In conclusion, Ni(OH)$_2$ HPA electrode exhibits advantages in both electron and mass transfer kinetics compared to Ni(OH)$_2$ BHPA. Figure 4c is the CVs of Ni(OH)$_2$ HPA electrode in 0.1 M NaOH with different glucose concentration at

Scheme 1 The schematic diagram of electrocatalytic mechanism

Fig. 5 a Amperometric response of Ni(OH)$_2$ HPA electrode at different potentials with the addition of 0.1 mM glucose and 0.01 mM AA. **b** The response current of glucose and AA at different potentials; **c** CA of Ni(OH)$_2$ HPA and Ni(OH)$_2$ BHPA electrodes at 0.6 V with the successive addition of glucose. **d** The relationship between response current and glucose concentration

50 mV/s. The oxidation peak current linearly increases with the glucose concentration (Fig. 4d), revealing applications in electrochemical glucose sensors. The CVs of Ni(OH)$_2$ HPA electrode with 0.5 mM glucose under different scan rates were recorded in Fig. 4e. As shown in Fig. 4f, the peak current linearly depends on the square root of scan rates, revealing diffusion controlled electrochemical process.

In order to confirm the optimized working potential, the current response of glucose and the interference of AA were considered at different potentials (Fig. 5a). From the statistics data displayed in Fig. 5b, Ni(OH)$_2$ HPA electrode exhibits minimum interference to AA and maximum current response to glucose at 0.6 V. Thus, 0.6 V was selected as the optimized working potential. Figure 5c shows the amperometric response curves of Ni(OH)$_2$ HPA and Ni(OH)$_2$ BHPA electrodes at 0.6 V. Ni(OH)$_2$ HPA electrode presents more sensitive response to glucose than Ni(OH)$_2$ BHPA electrode. Figure 5d is the corresponding calibration curves of Ni(OH)$_2$ HPA and Ni(OH)$_2$ BHPA electrodes. For Ni(OH)$_2$ HPA electrode, the results show a good linear region between 0.08 mM and 1.13 mM. The fitting equation is $y = 0.1296x + 16.486$ ($R_2 = 0.991$). By accurate calculation, Ni(OH)$_2$ HPA electrode has a sensitivity of 1843 μA mM^{-1} cm^{-2}, which is higher than Ni(OH)$_2$ BHPA electrode (632 μA mM^{-1} cm^{-2}). The detection limit of Ni(OH)$_2$ HPA electrode is calculated to be 0.23 μM (S/N = 3), which is lower than Ni(OH)$_2$ BHPA (0.67 μM). As displayed in Additional file 1: Figure S3, Ni(OH)$_2$ HPA electrode presents a shorter response time (1.4 s) compared to Ni(OH)$_2$ BHPA electrode (1.8 s). The analytical performances of Ni(OH)$_2$ HPA electrode are compared with other Ni(OH)$_2$-based electrodes, and the data are listed in Table 1. Notably, Ni(OH)$_2$ HPA electrode presents higher electroactivity towards glucose in terms of high sensitivity, low detection limit, and rapid response, indicating great potential applications as an electrochemical glucose detection electrode.

Common interferents in human blood, including Lact., Suct., Fruct., UA, and AA, are involved to evaluate the selectivity of Ni(OH)$_2$ HPA electrode [23]. As displayed in Fig. 6a, no more than 3.8% interferences are observed for all the interferents. The second current response for glucose retains 98.1% of its first signal. Figure 6b displays the amperometric response of Ni(OH)$_2$ HPA electrode towards 0.1 mM glucose within 2400 s at 0.60 V. The final response signal still retains approximately 93.5% of its original data, revealing an excellent long-term stability of Ni(OH)$_2$ HPA electrode. In Fig. 6c, current responses for one Ni(OH)$_2$ HPA electrode were tested for ten times. The signals display a relatively standard deviation (RSD) of 4.8%, demonstrating outstanding reproducibility. Moreover, the five Ni(OH)$_2$ HPA electrodes exhibit a satisfying RSD of 5.3%

Table 1 Comparison of researched electrode with reported nonenzymatic glucose sensors based on $Ni(OH)_2$

Electrode	Sensitivity ($\mu A\ mM^{-1}\ cm^{-2}$)	Detection limit (μM)	Response time (s)	Reference
$Ni(OH)_2$ HPA/GCE	1843	0.23	1.4	This work
$Ni(OH)_2$-CNT[a]-PVDF composite	–	23	3	[22]
$Ni(OH)_2$/nanoflowers	265.3	0.5	3	[24]
$Ni(OH)_2$/TiO_2	192.5	8	1	[25]
$Ni(OH)_2$ NP/MoS_x	162	5.8	2	[26]
Nano $Ni(OH)_2$ platelet-like	202	6	5–7	[27]
$Ni(OH)_2$/ECF[b]	1342.2	0.1	3	[28]
$Ni(OH)_2$-graphene	494	0.6	2	[29]
$Ni(OH)_2$@oPPyNW[c]	1049.2	0.3	10	[30]
$Ni(OH)_2$/Au/GCE	371.2	0.92	4	[31]

[a]Carbon nanotubes
[b]Electrospun carbon nanofiber
[c]Over-oxidized polypyrrole nanowires

(Fig. 6d). $Ni(OH)_2$ HPA electrode possesses excellent selectivity, satisfying stability and reproducibility, demonstrating attractive applications in electrochemical glucose sensors.

Conclusions

We have used a facile strategy inspired by the CEP principle to controllably fabricate uniform $Ni(OH)_2$ HPA at room temperature. $Ni(OH)_2$ HPA presents large SSA, ordered diffusion channels, and high structure stability. As a electrochemical detection electrode for glucose, $Ni(OH)_2$ HPA exhibits higher sensitivity of 1843 $\mu A\ mM^{-1}\ cm^{-2}$, faster response time (1.4 s), and lower detection limit of 0.23 μM compared to broken sample (1.8 s, 0.67 μM). The $Ni(OH)_2$ HPA electrode presents improved electrochemical sensing performance towards glucose, revealing promising feature for the practical analytical application. The hollow porous architecture is also confirmed as an effective strategy to obtain high-performance electrocatalysts.
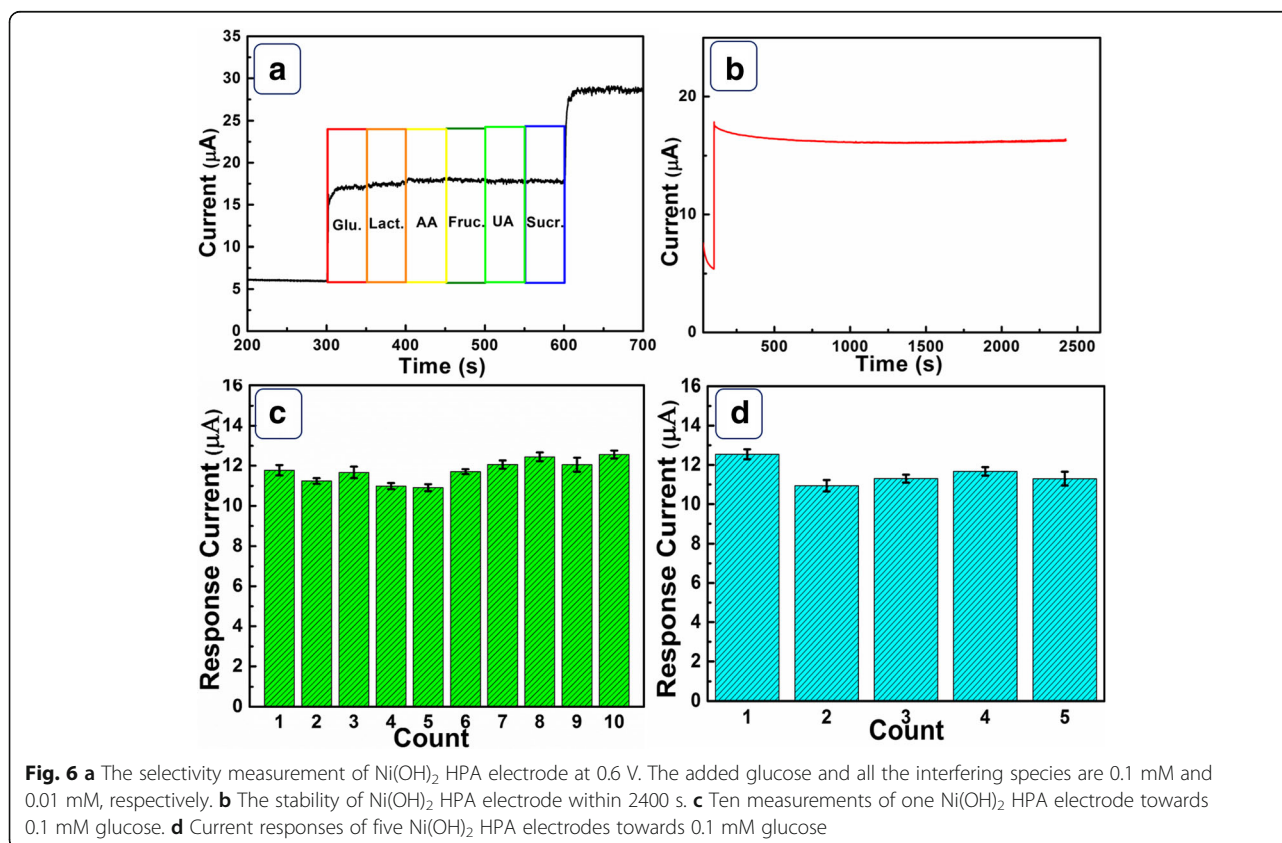

Fig. 6 a The selectivity measurement of $Ni(OH)_2$ HPA electrode at 0.6 V. The added glucose and all the interfering species are 0.1 mM and 0.01 mM, respectively. **b** The stability of $Ni(OH)_2$ HPA electrode within 2400 s. **c** Ten measurements of one $Ni(OH)_2$ HPA electrode towards 0.1 mM glucose. **d** Current responses of five $Ni(OH)_2$ HPA electrodes towards 0.1 mM glucose

Additional file

Abbreviations
AA: L-ascorbic acid; BET: Brunauer-Emmett-Teller; CA: Chronoamperometry; CEP: Coordinating etching and precipitating; CNT: Carbon nanotubes; ECF: Electrospun carbon nanofiber; EIS: Electrochemical impedance spectroscopy; FESEM: Field emission scanning electron microscope; Fruc.: Fructose; GCE: Glassy carbon electrode; Glu.: Glucose; HPA: Hollow porous architecture; Lact.: Lactose; $Ni(OH)_2$ BHPA: Broken $Ni(OH)_2$ HPA; oPPyNW: Over-oxidized polypyrrole nanowires; PVP: Polyvinyl pyrrolidone; *Rct*: Electron transfer resistance; *Rs*: Internal resistance; RSD: Relatively standard deviation; SAED: Selected area electron diffraction; SSA: Specific surface area; Sucr.: Sucrose; UA: Uric acid; XPS: X-ray photoelectron spectrometer; XRD: X-ray diffraction; *Zw*: Warburg impedance

Availability of Data and Materials
The datasets are available without restriction.

Authors' Contributions
LLT design the experiment and wrote the paper. GGH and YCY did the electrochemical measurements. XB prepared the materials and made the characterizations. MJC and JBW provided financial supports. All authors read and approved the final manuscript.

Competing Interests
The authors declare that they have no competing interests.

Publisher's Note
Springer Nature remains neutral with regard to jurisdictional claims in published maps and institutional affiliations.

Author details
[1]Research Institute for New Materials Technology, Chongqing University of Arts and Sciences, Chongqing, People's Republic of China. [2]School of Science, MOE Key Laboratory for Non-equilibrium Synthesis and Modulation of Condensed Matter, State Key Laboratory for Mechanical Behavior of Materials, Xi'an Jiaotong University, Xi'an, People's Republic of China.

References
1. Heller A, Feldman B (2008) Electrochemical glucose sensors and their application in diabetes management. Chem Rev 108:2482–2505
2. Noh HB, Lee KS, Chandra P, Won MS, Shim YB (2012) Application of a Cu-Co alloy dendrite on glucose and hydrogen peroxide sensors. Electrochim Acta 61:36–43
3. Wang MQ, Ye C, Bao SJ, Xu MW, Zhang Y, Wang L, Ma XQ, Guo J, Li CM (2017) Nanostructured cobalt phosphates as excellent biomimetic enzymes to sensitively detect superoxide anions released from living cells. Biosens Bioelectron 87:998–1004
4. Hsieh HV, Pfeiffer ZA, Amiss TJ, Sherman DB, Pitner JB (2004) Direct detection of glucose by surface plasmon resonance with bacterial glucose/galactose-binding protein. Biosens Bioelectron 19:653–660
5. Jiang Z, Huang Y, Liang A, Pan H, Liu Q (2009) Resonance scattering detection of trace microalbumin using immunonanogold probe as the catalyst of Fehling reagent-glucose reaction. Biosens Bioelectron 24:1674–1678
6. Da SC, Mennucci B, Vreven T (2004) Density functional study of the optical rotation of glucose in aqueous solution. J Org Chem 69:8161–8164
7. Moschou EA, Sharma BV, Deo SK, Daunert S (2004) Fluorescence glucose detection: advances toward the ideal in vivo biosensor. J Fluoresc 14:535–547
8. Yu X, Xu J, Lu H, Fang G (2017) Sol-gel derived Al-doped zinc oxide-reduced graphene oxide nanocomposite thin films. J Alloys Compd 699:79–86
9. Bao S, Li CM, Zang J, Cui X, Qiao Y, Guo J (2010) New nanostructured TiO_2 for direct electrochemistry and glucose sensor applications. Adv Funct Mater 18:591–599
10. Wang J (2008) Electrochemical glucose biosensors. Chem Rev 108:814–825
11. Mcintyre NS, Cook MG (1975) X-ray photoelectron studies on some oxides and hydroxides of cobalt, nickel, and copper. Anal Chem 47:2208–2213
12. Biesinger MC, Payne BP, Lau LWM, Gerson A, Smart RSC (2010) X-ray photoelectron spectroscopic chemical state quantification of mixed nickel metal, oxide and hydroxide systems. Surf Interface Anal 41:324–332
13. Cao CY, Guo W, Cui ZM, Song WG, Cai W (2011) Microwave-assisted gas/liquid interfacial synthesis of flowerlike NiO hollow nanosphere precursors and their application as supercapacitor electrodes. J Mater Chem 21:3204–3209
14. Ci S, Huang T, Wen Z, Cui S, Mao S, Steeber DA, Chen J (2014) Nickel oxide hollow microsphere for non-enzyme glucose detection. Biosens Bioelectron 54:251–257
15. Xu Y, Tu W, Zhang B, Yin S, Huang Y, Kraft M, Xu R (2017) Nickel nanoparticles encapsulated in few-layer nitrogen-doped graphene derived from metal-organic frameworks as efficient bifunctional electrocatalysts for overall water splitting. Adv Mater 29:1605957
16. Payne BP, Biesinger MC, Mcintyre NS (2009) The study of polycrystalline nickel metal oxidation by water vapour. J Electron Spectrosc Relat Phenom 175:55–65
17. Tian L, Zhong X, Hu W, Liu B, Li Y (2014) Fabrication of cubic PtCu nanocages and their enhanced electrocatalytic activity towards hydrogen peroxide. Nanoscale Res Lett 9:68–68
18. Xia K, Yang C, Chen Y, Tian L, Su Y, Wang J, Li L (2016) In situ fabrication of $Ni(OH)_2$ flakes on Ni foam through electrochemical corrosion as high sensitive and stable binder-free electrode for glucose sensing. Sensors Actuators B Chem 240:979–987
19. Sun S, Yang Z (2014) Cu_2O-templated strategy for synthesis of definable hollow architectures. Chem Commun 50:7403–7415
20. Sohn JH, Cha HG, Kim CW, Kim dK, Kang YS (2013) Fabrication of hollow metal oxide nanocrystals by etching cuprous oxide with metal(ii) ions: approach to the essential driving force. Nanoscale 5:11227–11233
21. Zhao Y, Song X, Song Q, Yin Z (2012) A facile route to the synthesis copper oxide/reduced graphene oxide nanocomposites and electrochemical detection of catechol organic pollutant. Crystengcomm 14:6710–6719
22. Yan X, Gao G, Zhu G, Gao J, Ge Z, Yang H (2014) A nonenzymatic electrochemical glucose sensor based on $Ni(OH)_2$-cnt-pvdf composite and its application in measuring serum glucose. J Electrochem Soc 161:B106–B110
23. Liu M, Liu R, Chen W (2013) Graphene wrapped Cu_2O nanocubes: non-enzymatic electrochemical sensors for the detection of glucose and hydrogen peroxide with enhanced stability. Biosens Bioelectron 45:206–212
24. Yang H, Gao G, Teng F, Liu W, Chen S, Ge Z (2014) Nickel hydroxide nanoflowers for a nonenzymatic electrochemical glucose sensor. J Electrochem Soc 161:B216–B219
25. Gao A, Zhang X, Peng X, Wu H, Bai L, Jin W, Wu G, Hang R, Chu PK (2016) In situ synthesis of $Ni(OH)_2/TiO_2$ composite film on NiTi alloy for non-enzymatic glucose sensing. Sensors Actuators B Chem 232:150–157
26. Ji S, Yang Z, Zhang C, Miao Y-E, Liu T (2013) Nonenzymatic sensor for glucose based on a glassy carbon electrode modified with $Ni(OH)_2$ nanoparticles grown on a film of molybdenum sulfide. Microchim Acta 180:1127–1134
27. Safavi A, Maleki N, Farjami E (2009) Fabrication of a glucose sensor based on a novel nanocomposite electrode. Biosens Bioelectron 24:1655–1660
28. Chen L, Liu L, Guo Q, Wang Z, Liu G, Chen S, Hou H (2017) Preparation of $Ni(OH)_2$ nanoplatelet/electrospun carbon nanofiber hybrids for highly sensitive nonenzymatic glucose sensors. RSC Adv 7:19345–19352

Tian *et al. Nanoscale Research Letters*   (2018) 13:342

Page 9 of 9

29. Qiao N, Zheng J (2012) Nonenzymatic glucose sensor based on glassy carbon electrode modified with a nanocomposite composed of nickel hydroxide and graphene. Microchim Acta 177:103–109
30. Yang J, Cho M, Pang CH, Lee Y (2015) Highly sensitive non-enzymatic glucose sensor based on over-oxidized polypyrrole nanowires modified with Ni(OH)$_2$ nanoflakes. Sensors Actuators B Chem 211:93–101
31. Chen J, Zheng J (2015) A highly sensitive non-enzymatic glucose sensor based on tremella-like Ni(OH)$_2$ and Au nanohybrid films. J Electroanal Chem 749:83–88